

Thermoelectric $\text{Si}_{1-x}\text{Ge}_x$ and Ge epitaxial films on Si(001) with controlled composition and strain for group IV element-based thermoelectric generators

Cite as: Appl. Phys. Lett. **117**, 141602 (2020); <https://doi.org/10.1063/5.0023820>

Submitted: 01 August 2020 . Accepted: 19 September 2020 . Published Online: 05 October 2020

Tatsuhiko Taniguchi, Takafumi Ishibe, Ryoya Hosoda, Youya Wagatsuma, Md. Mahfuz Alam, Kentarou Sawano, Mutsunori Uenuma, Yukiharu Uraoka, Yuichiro Yamashita , Nobuya Mori, and Yoshiaki Nakamura 



View Online



Export Citation



CrossMark

ARTICLES YOU MAY BE INTERESTED IN

Low temperature homoepitaxy of (010) $\beta\text{-Ga}_2\text{O}_3$ by metalorganic vapor phase epitaxy: Expanding the growth window

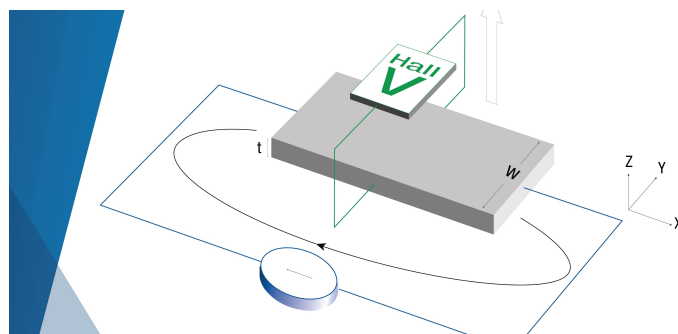
Applied Physics Letters **117**, 142102 (2020); <https://doi.org/10.1063/5.0023778>

Trapping of multiple H atoms at the Ga(I) vacancy in $\beta\text{-Ga}_2\text{O}_3$

Applied Physics Letters **117**, 142101 (2020); <https://doi.org/10.1063/5.0024269>

Temperature-dependent phase noise properties of a two-section GaSb-based mode-locked laser emitting at $2\ \mu\text{m}$

Applied Physics Letters **117**, 141103 (2020); <https://doi.org/10.1063/5.0024064>



**Tips for minimizing
Hall measurement errors**

Download the Technical Note

Lake Shore
CRYOTRONICS

Thermoelectric $\text{Si}_{1-x}\text{Ge}_x$ and Ge epitaxial films on Si(001) with controlled composition and strain for group IV element-based thermoelectric generators

Cite as: Appl. Phys. Lett. **117**, 141602 (2020); doi: [10.1063/5.0023820](https://doi.org/10.1063/5.0023820)

Submitted: 1 August 2020 · Accepted: 19 September 2020 ·

Published Online: 5 October 2020




View Online



Export Citation



CrossMark

Tatsuhiko Taniguchi,¹ Takafumi Ishibe,¹ Ryoya Hosoda,¹ Youya Wagatsuma,² Md. Mahfuz Alam,² Kentarou Sawano,² Mutsunori Uenuma,³ Yukiharu Uraoka,³ Yuichiro Yamashita,⁴  Nobuya Mori,⁵ and Yoshiaki Nakamura^{1,a)} 

AFFILIATIONS

¹Graduate School of Engineering Science, Osaka University, 1-3 Machikaneyama-cho, Toyonaka, Osaka 560-8531, Japan

²Advanced Research Laboratories, Tokyo City University, Setagaya, Tokyo 158-0082, Japan

³Division of Materials Science, Nara Institute of Science and Technology, 8916-5 Takayama, Ikoma, Nara 630-0192, Japan

⁴National Institute of Advanced Industrial Science and Technology, Tsukuba, Ibaraki 305-8565, Japan

⁵Graduate School of Engineering, Osaka University, 2-1 Yamadaoka, Suita, Osaka 565-0871, Japan

^{a)}Author to whom correspondence should be addressed: nakamura@ee.es.osaka-u.ac.jp

ABSTRACT

This study presents the material design of $\text{Si}_{1-x}\text{Ge}_x$ epitaxial films/Si for thin film thermoelectric generators (TFTEGs) by investigating their thermoelectric properties. The thermoelectric films composed of group-IV elements are advantageous due to their compatibility with the Si process. We fabricated $\text{Si}_{1-x}\text{Ge}_x$ epitaxial films with various controlled x values and strains using various growth methods. Ge epitaxial films without strains exhibited the highest thermoelectric power factor ($\sim 47 \mu\text{W cm}^{-1} \text{K}^{-2}$) among various strain-controlled $\text{Si}_{1-x}\text{Ge}_x$ ($x \neq 1$) epitaxial films, which is higher at room temperature than SiGe alloy-based bulks ever reported. On the other hand, strained $\text{Si}_{1-x}\text{Ge}_x$ epitaxial films showed an ultralow thermal conductivity of $\sim 2 \text{W m}^{-1} \text{K}^{-1}$, which is close to the value for amorphous Si. In addition to strained SiGe films with the ultralow thermal conductivity, unstrained Ge films with a high thermoelectric power factor can also be used for future TFTEGs by applying a nanostructuring technique. A preliminary TFTEG of Ge epitaxial films was realized, which generated a maximum power of $\sim 0.10 \mu\text{W cm}^{-2}$ under a temperature difference of 20 K. This demonstrates that epitaxial films composed of group-IV semiconductors are promising materials for TFTEG applications.

Published under license by AIP Publishing. <https://doi.org/10.1063/5.0023820>

Thermoelectric generators (TEGs), which enable us to reuse a vast amount of waste heat, are attracting great interest as one of the sustainable energy sources.^{1–3} The thermoelectric (TE) conversion efficiency of the materials is evaluated by the dimensionless figure-of-merit $ZT (=S^2\sigma T/\kappa)$, where S is the Seebeck coefficient, σ is the electrical conductivity, T is the absolute temperature, and κ is the thermal conductivity. Considerable effort has been made on developing high ZT materials,^{4–18} namely, the simultaneous realization of high power factor $S^2\sigma$ and low κ . A large temperature difference ΔT and high $S^2\sigma$ are important for obtaining a large output power from the thin film TEG (TFTEG). To obtain a sufficient ΔT , there were a lot of pronounced reports about the κ reduction of TE films by nanostructuring with almost no degradation of high $S^2\sigma$, for example, through the fabrication of holes or nanodots in the films using the Si process technique.^{19–21} Now, thin films with high $S^2\sigma$ are gaining importance

when they are compatible with the Si process technique to use the nanostructuring technique for κ reduction.

Group-IV semiconductors, such as Si, are suitable for the industry because of their eco-friendly and non-toxic properties. In the TE research field, there have been a lot of studies about bulk $\text{Si}_{1-x}\text{Ge}_x$ ^{8,9,27–29} and polycrystalline $\text{Si}_{1-x}\text{Ge}_x$ films.^{4,12,14} $\text{Si}_{1-x}\text{Ge}_x$ ($0 < x \leq 1$) TE films on Si substrates are compatible with Si technology,^{17,22–26} which has aided the realization of various digital devices, where the carrier mobility μ was effectively controlled by varying x and the hetero-epitaxial strain. There are many TE studies on Si-based superlattice films.^{18,30–32} On the other hand, the “ $\text{Si}_{1-x}\text{Ge}_x$ epitaxial films” on Si substrates, which can give basic character depending on x and strain, have not been experimentally investigated in terms of “TE properties” except for our previous work about p-type Ge epitaxial films;³³ despite their advantages, a lot of information exists about group-IV semiconductors, their good properties

(high S and μ), and their compatibility with industry. The epitaxial films have intermixed layers, strains, and dislocations at the hetero-interfaces between the $\text{Si}_{1-x}\text{Ge}_x$ films and Si substrates, which influence carrier and phonon transports related to the TE properties. Moreover, the Ge composition x has an impact on the electronic states of $\text{Si}_{1-x}\text{Ge}_x$. The TE properties of epitaxial films are not sufficiently simple to be predicted in the same manner as bulk $\text{Si}_{1-x}\text{Ge}_x$. For group IV element-based TFTEGs, it is necessary to clarify the TE properties of $\text{Si}_{1-x}\text{Ge}_x$ epitaxial films depending on the strain and composition.

In this study, we establish a material design of $\text{Si}_{1-x}\text{Ge}_x$ epitaxial films/Si for TFTEG applications. $\text{Si}_{1-x}\text{Ge}_x$ epitaxial films with various controlled x values and strain are fabricated using two kinds of growth methods. Ge epitaxial films exhibit the highest $S^2\sigma$ ($\sim 47 \mu\text{W cm}^{-1} \text{K}^{-2}$) among the strain-controlled SiGe epitaxial films, which is higher than those of the n-type SiGe-alloy-based bulks that have been ever reported at room temperature.³⁴ On the other hand, $\text{Si}_{0.7}\text{Ge}_{0.3}$ films display ultralow κ ($\sim 2 \text{ W m}^{-1} \text{K}^{-1}$). Thus, SiGe epitaxial films are suitable due to the ultralow κ , and Ge epitaxial films with higher $S^2\sigma$ can also be a material candidate for TFTEG applications by applying the nanostructuring technique in the future to generate sufficient ΔT . The preliminary TFTEG of the Ge epitaxial film is realized and generates a maximum power of $\sim 0.10 \mu\text{W cm}^{-2}$ under a ΔT value of 20 K. This demonstrates that $\text{Si}_{1-x}\text{Ge}_x$ epitaxial films/Si can be promising TFTEG materials.

Strained and unstrained $\text{Si}_{1-x}\text{Ge}_x$ epitaxial films were fabricated on Si substrates using one-step and two-step growth, respectively, in the following manner.^{35,36} Chemically cleaned undoped Si(001) substrates (electrical resistivity: $\geq 1000 \Omega \text{ cm}$) were introduced into a molecular beam epitaxy (MBE) chamber at a base pressure of $\sim 1 \times 10^{-8} \text{ Pa}$, equipped with Knudsen cells for Si and Ge. After degassing the substrates at 550°C for $\sim 5 \text{ h}$, 50 nm Si buffer layers were formed on the Si substrates at 500°C to obtain the clean Si(001)-(2 \times 1) reconstructed surfaces. In the case of one-step growth [without the low-temperature (LT)-grown $\text{Si}_{1-x}\text{Ge}_x$ buffer layer], the $\text{Si}_{1-x}\text{Ge}_x$ films ($x = 0.3, 0.5$) were directly grown on the Si buffer layers at 400°C . In the case of two-step growth (with the LT-grown $\text{Si}_{1-x}\text{Ge}_x$ buffer layer), the $\text{Si}_{1-x}\text{Ge}_x$ buffer layers with a thickness of 50 nm were grown on the Si buffer layers at a LT of 100°C . These LT-grown $\text{Si}_{1-x}\text{Ge}_x$ buffer layers work as strain-relaxation layers between the $\text{Si}_{1-x}\text{Ge}_x$ films and the Si substrates. Subsequently, the $\text{Si}_{1-x}\text{Ge}_x$ films ($x = 0.3, 1$) were grown at 400°C on the LT-grown $\text{Si}_{1-x}\text{Ge}_x$ buffer layers. The samples fabricated using the one-step and two-step growth methods are referred to as one-step and two-step $\text{Si}_{1-x}\text{Ge}_x$ samples, respectively. The two-step $\text{Si}_{1-x}\text{Ge}_x$ samples were expected to be

strain-relaxed, while the one-step growth samples were considered to be strained. For n-type doping, ion implantation was carried out using a phosphorous ion beam with ion kinetic energies of 25–30 keV. The dose was in the range of 1×10^{14} – $1 \times 10^{15} \text{ cm}^{-2}$. To electrically activate phosphorous atoms, the doped samples were annealed at 400°C ($x = 1$) or 500°C ($x = 0.3, 0.5$) for 10 min at a N_2 flow rate of $\sim 0.5 \text{ l min}^{-1}$. The thickness of the doped layer (DL) (carrier conducting layer) was defined as the ion implantation depth estimated from the stopping and range of ions in matter (SRIM) calculation.¹⁸ The fabricated samples are summarized in Table I, where the film thickness in the case of two-step samples does not include the thickness of the LT-grown $\text{Si}_{1-x}\text{Ge}_x$ buffer layers.

In situ reflection high-energy electron diffraction (RHEED) observations were performed with a 20 keV electron beam incident in the $\langle 110 \rangle_{\text{Si}}$ direction. Atomic force microscopy (AFM) observations were performed with the Si cantilevers. Reciprocal space maps (RSMs) were obtained by *ex situ* x-ray diffraction (XRD) measurements with a Cu K α line (wavelength: 0.15418 nm). The carrier concentration n , σ , and S values were measured in the in-plane direction using Hall effect measurements, the van der Pauw method, and the Seebeck coefficient measurement system (ADVANCE-RIKO ZEM-3), respectively. The κ values in the cross-plane direction were measured at room temperature using the front-heating/front-detection time domain thermoreflectance (TDTR) method. Mo transducer films with thicknesses of $\sim 150 \text{ nm}$ and $\sim 100 \text{ nm}$ were deposited on the undoped and doped samples, respectively, for detecting the thermoreflectance signal.

The unileg-type TFTEG was fabricated using the Ge sample. Ge stripe structures with dimensions of $4 \text{ mm} \times 450 \mu\text{m} \times 100 \text{ nm}$ were fabricated using photolithography and dry etching using CH_4 , O_2 , and He. The stripe interval was designed to be $\sim 150 \mu\text{m}$. To connect the Ge stripe structures electrically in series, Al electrodes with a width of $100 \mu\text{m}$ and a thickness of 150 nm were fabricated by photolithography and electron beam deposition. During the measurement of the TFTEG characteristics near room temperature, ΔT between the hot and cold sides was created by Peltier devices and evaluated using an InSb detector (InfraScope MWIR temperature mapping microscope, Quantum Focus Instruments Co.).³⁷

Figure 1 shows the AFM images and RHEED patterns (insets) of the one-step [Fig. 1(a)] and two-step $\text{Si}_{0.7}\text{Ge}_{0.3}$ samples with a thickness of 150 nm [Fig. 1(b)], which are typical surface morphologies and diffraction patterns of the one-step and two-step samples. In all the samples, RHEED patterns with (2×1) surface reconstruction were observed, indicating that all the $\text{Si}_{1-x}\text{Ge}_x$ samples were epitaxially grown on Si(001) substrates. However, the surface morphologies of

TABLE I. Film thickness and doped layer (DL) thickness estimated from the SRIM calculation, Ge composition x , and in-plane strain $\varepsilon_{//}$ of the DLs measured from the RSMs of the doped samples.

Sample name	Target film thickness (nm)	Measured film thickness (nm)	DL thickness (nm)	Target x		$\varepsilon_{//}$ of the DL (sample with n)
				Target x	Measured x	
One-step $\text{Si}_{0.7}\text{Ge}_{0.3}$ sample (100 nm)	100	92	78	0.3	0.23	-0.67% ($\sim 4.1 \times 10^{19} \text{ cm}^{-3}$)
One-step $\text{Si}_{0.7}\text{Ge}_{0.3}$ sample (150 nm)	150	137	91	0.3	0.26	-0.23% ($\sim 6.7 \times 10^{19} \text{ cm}^{-3}$)
Two-step $\text{Si}_{0.7}\text{Ge}_{0.3}$ sample	150	130	91	0.3	0.25	-0.05% ($\sim 8.4 \times 10^{19} \text{ cm}^{-3}$)
One-step $\text{Si}_{0.5}\text{Ge}_{0.5}$ sample	100	100	78	0.5	0.38	-0.02% ($\sim 8.9 \times 10^{19} \text{ cm}^{-3}$)
Two-step Ge sample	100	79	71	1.0	1.00	-0.01% ($\sim 2.8 \times 10^{19} \text{ cm}^{-3}$)

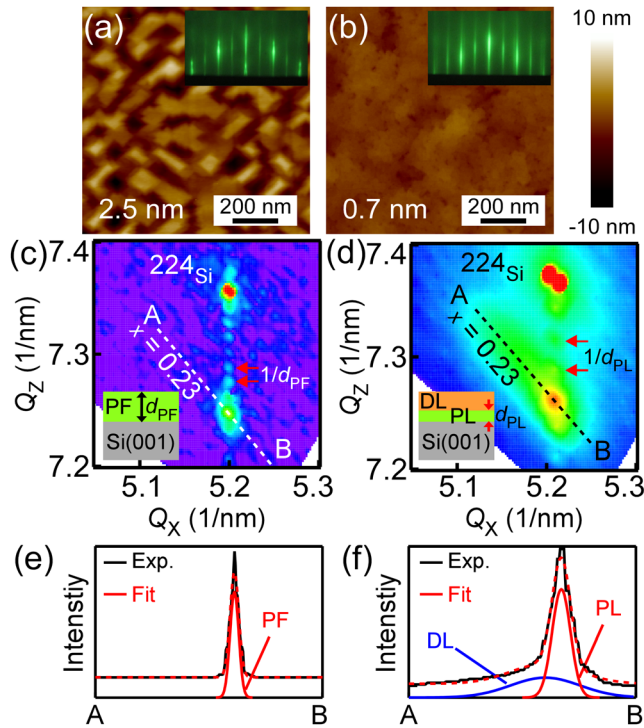


FIG. 1. AFM images of (a) one-step $\text{Si}_{0.7}\text{Ge}_{0.3}$ sample (150 nm) and (b) two-step $\text{Si}_{0.7}\text{Ge}_{0.3}$ sample. RMS values of surface morphologies are described. The insets show the corresponding RHEED patterns. (c) and (d) RSMs of the (c) as-grown and (d) doped one-step $\text{Si}_{0.7}\text{Ge}_{0.3}$ samples (100 nm). (e) and (f) Profiles along the dashed lines from A to B in (c) and (d), respectively.

the one-step and two-step $\text{Si}_{1-x}\text{Ge}_x$ samples seemed to be quite different. AFM observation indicated that the root mean square (RMS) values of the surface morphologies are 2.5 nm for the one-step $\text{Si}_{0.7}\text{Ge}_{0.3}$ sample and 0.7 nm for the two-step $\text{Si}_{0.7}\text{Ge}_{0.3}$ sample, which are consistent with the spotty and streaky diffraction spots in RHEED patterns, respectively. This result of surface roughness implies the film strain difference between the one-step and two-step samples.

Figures 1(c) and 1(d) show the RSMs of the as-grown (undoped) and doped ($n \sim 4.1 \times 10^{19} \text{ cm}^{-3}$) one-step $\text{Si}_{0.7}\text{Ge}_{0.3}$ samples with a thickness of 100 nm as typical examples. Pendellösung fringes were observed between the 224_{Si} spots from the Si substrate and the 224_{SiGe} spots from the $\text{Si}_{0.7}\text{Ge}_{0.3}$ film, indicating pseudomorphic growth. The profiles crossing the 224_{SiGe} spot peaks were acquired along the dashed lines corresponding to an x value of 0.23 in Figs. 1(c) and 1(d), as shown in Figs. 1(e) and 1(f), respectively. In the as-grown sample, one sharp peak fitted with one Gaussian function was observed as shown in Fig. 1(e), and the Pendellösung fringe separation in Fig. 1(c) corresponds to the thickness of the pseudomorphic film (PF) of ~ 100 nm (d_{PF}). However, in the case of the doped samples, the 224_{SiGe} diffraction peak was fitted with two Gaussian functions: one broad and one sharp [Fig. 1(f)]. The sharp peak position in Fig. 1(f) is similar to that of the PF in Fig. 1(e). From these results, it was found that the doped sample has the two layers [the doped layer (DL) and pseudomorphic layer (PL)] corresponding to two diffraction peaks because the DL was formed by ion implantation to the as-grown PF (~ 100 nm), as shown

in the schematic in the insets in Figs. 1(c) and 1(d). Actually, the fringe separation was changed by ion implantation and corresponds to a smaller thickness (~ 38 nm) of the PL (d_{PL}) [Fig. 1(d)]. This revealed that the DL with some strain relaxation formed by ion implantation has a thickness of ~ 62 nm, which is approximately equal to the ion implantation depth. Using the broad fitted Gaussian curve of the DL [Fig. 1(f)], its x and in-plane strain (ϵ_{\parallel}) were estimated to be 0.23 and $\sim -0.67\%$, respectively. The analysis results and the RSMs of the other samples are summarized in Table I and in Figs. S1 and S2 in the supplementary material, respectively. It was found that the thicker one-step samples (150 nm thickness) are relatively strain-relaxed and the two-step samples and higher x samples were almost completely strain-relaxed. These results demonstrated that strained and unstrained $\text{Si}_{1-x}\text{Ge}_x$ films were well grown on Si substrates epitaxially.

We measured the TE properties of the $\text{Si}_{1-x}\text{Ge}_x$ samples with various x and ϵ_{\parallel} values at room temperature. Figure 2(a) shows the values of σ as a function of n . Each sample exhibited a lower σ value than each bulk [the semi-empirical curves of bulk materials (see the supplementary material, Sec. II) indicated by the solid curves in Figs. 2(a) and 2(b)].^{38,39} The degradation of σ from the bulk values could be attributed to large amounts of defects originating from growth temperatures lower than bulk growth cases (~ 800 – 1200 °C). As shown in Fig. 2(a), Ge samples exhibited higher σ values than those of the $\text{Si}_{0.7}\text{Ge}_{0.3}$ and $\text{Si}_{0.5}\text{Ge}_{0.5}$ samples. This is because the conductivity effective mass (m_c) of Ge ($0.12 m_0$, where m_0 is the free electron mass) is smaller than those of $\text{Si}_{0.7}\text{Ge}_{0.3}$ and $\text{Si}_{0.5}\text{Ge}_{0.5}$ ($0.26 m_0$),⁴⁰ in addition to the alloy scattering of electrons in $\text{Si}_{0.7}\text{Ge}_{0.3}$ and $\text{Si}_{0.5}\text{Ge}_{0.5}$ samples. The μ values of $\text{Si}_{1-x}\text{Ge}_x$ samples ($x \neq 1$) are plotted as a function of n , as shown in Fig. 2(b). The strained one-step $\text{Si}_{0.7}\text{Ge}_{0.3}$ samples exhibited higher μ values than the other samples with less strain. In general, the strain causes degeneracy lifting from sixfold to two- and fourfold degeneracies in the Si–Ge system.^{40,41} In the case of compressively strained $\text{Si}_{1-x}\text{Ge}_x$ ($x < 0.85$), carriers predominantly transport in the fourfold degenerate bands with smaller m_c , positioning at lower energy levels. This small m_c explains the higher μ values of the one-step $\text{Si}_{0.7}\text{Ge}_{0.3}$ samples (100 nm). These results highlight that in terms of σ , the Ge samples and the compressively strained $\text{Si}_{1-x}\text{Ge}_x$ samples with small x are better owing to the smaller m_c .

To investigate the compositional effect on the S values, the n – S data of the less-strained samples with various x values (0.3, 0.5, and 1) are plotted, namely, unstrained two-step $\text{Si}_{1-x}\text{Ge}_x$ ($x = 0.3, 1$) and one-step $\text{Si}_{1-x}\text{Ge}_x$ ($x = 0.5$) samples. In the region $n > 1 \times 10^{19} \text{ cm}^{-3}$, there was a significant difference in the S values: $\text{Si}_{0.7}\text{Ge}_{0.3}$ (triangles) $>$ $\text{Si}_{0.5}\text{Ge}_{0.5}$ (rhombi) $>$ Ge (squares). The theoretical S curves were computed based on the Boltzmann transport equation under the relaxation time and effective mass approximation,^{16–18,42} where two carrier scattering processes were assumed: ionized impurity scattering (for all samples) and alloy scattering (not for Ge samples). The relaxation time (τ) of the ionized impurity scattering process⁴³ is described as $16\pi\alpha^2(2m_d)^{1/2}E^{3/2}/q^4n$, where q is the elementary charge, E is the carrier energy, α is the permittivity, and m_d is the density-of-state (DOS) effective mass. τ for the alloy scattering process⁴⁴ is described as $64/[3\pi^2x(1-x)a^3U_0D(E)]$, where a is the lattice constant, U_0 is the alloy scattering potential (0.8 eV for Si–Ge alloy), $D(E)$ is the DOS of the conduction band, and \hbar is the Dirac constant. $D(E)$ is given by a simple parabolic band model as follows: $D(E) = (2m_d^3)^{1/2}E^{1/2}/\pi^2\hbar^3$. Considering the influence of the band structure on the S value, we

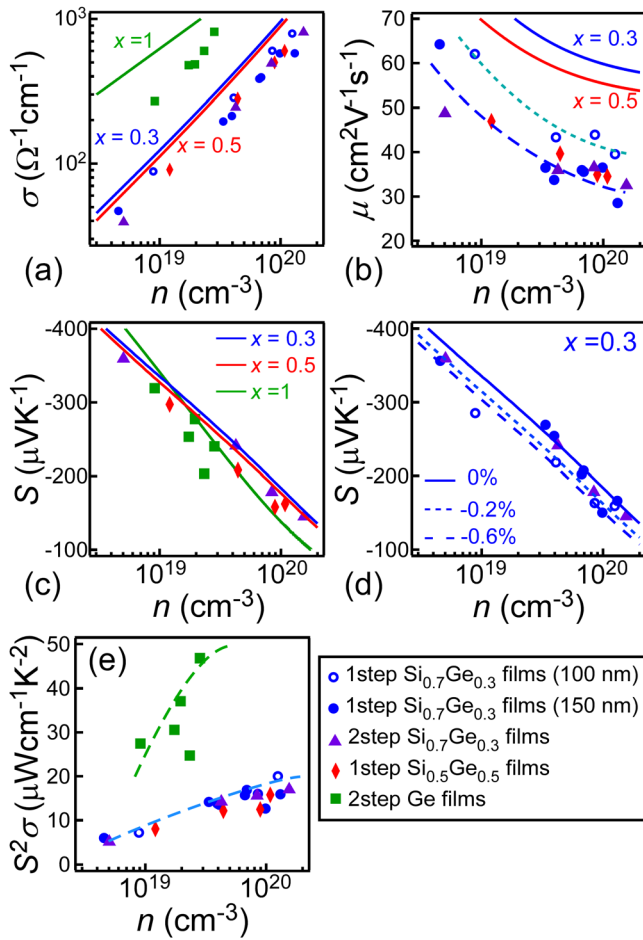


FIG. 2. (a)–(e) n dependences of (a) σ , (b) μ , (c) and (d) S , and (e) $S^2\sigma$ at room temperature. The solid curves in (a) and (b) are the semi-empirical curves of $\text{Si}_{1-x}\text{Ge}_x$ ($x = 1, 0.3$, and 0.5). The dotted and dashed curves in (b) are given as guides to the eye of the strained one-step $\text{Si}_{0.7}\text{Ge}_{0.3}$ samples (100 nm) (dotted) and the other less-strained $\text{Si}_{0.7}\text{Ge}_{0.3}$ samples (dashed). The solid lines in (c) are the theoretical S curves of almost-unstrained $\text{Si}_{1-x}\text{Ge}_x$ films with various x values ($0.3, 0.5$, and 1). The solid, dotted, and dashed curves in (d) are the theoretical S curves of $\text{Si}_{0.7}\text{Ge}_{0.3}$ films with various strains ($\epsilon_{||} = 0\%$, -0.2% , and -0.6% , respectively). The theoretical S curves were computed based on the Boltzmann transport equation under relaxation time and effective mass approximation. The dashed curves in (e) are given as guides to the eye.

used the following effective density of state (N_C): $1.04 \times 10^{19} \text{ cm}^{-3}$ for Ge and $2.80 \times 10^{19} \text{ cm}^{-3}$ for unstrained $\text{Si}_{0.7}\text{Ge}_{0.3}$ and $\text{Si}_{0.5}\text{Ge}_{0.5}$, which are determined by the degree of degeneracy and m_d . The theoretical S curves reproduce the experimental n - S plots well, as shown in Fig. 2(c), although a little smaller S in the case of $\text{Si}_{0.5}\text{Ge}_{0.5}$ was observed presumably due to the crystal defects caused by the strain relaxation in the one-step growth. From this computation, the fact that unstrained $\text{Si}_{1-x}\text{Ge}_x$ exhibited higher S values than Ge samples is accounted for by the larger N_C of unstrained $\text{Si}_{1-x}\text{Ge}_x$ than Ge samples.

We investigated the effect of $\epsilon_{||}$ on the S values of the $\text{Si}_{0.7}\text{Ge}_{0.3}$ samples, as shown in Fig. 2(d). The almost-unstrained two-step

samples with an $\epsilon_{||}$ value of -0.05% (triangles) and less-strained thick samples with an $\epsilon_{||}$ value of -0.23% (solid circles) exhibited S values higher than more-strained one-step thin samples with an $\epsilon_{||}$ value of -0.67% (open circles) in Fig. 2(d). To explain this strain-induced S reduction, the theoretical S curves were calculated in a manner similar to those in Fig. 2(c), using individual N_C values: $2.80 \times 10^{19} \text{ cm}^{-3}$ (unstrained), $2.20 \times 10^{19} \text{ cm}^{-3}$ ($\epsilon_{||} \sim -0.2\%$), and $1.95 \times 10^{19} \text{ cm}^{-3}$ ($\epsilon_{||} \sim -0.6\%$).⁴¹ In these calculations, $\epsilon_{||} = -0.2\%$ causes S reduction (dotted curve), which cannot explain the experimental results of the samples with $\epsilon_{||} = -0.23\%$ (solid circles). It is difficult to predict the effect of strain on TE properties using such a simple calculation. However, the strain-induced S reduction can be easily understood qualitatively because strain lifts the degeneracy of the electronic state near the conduction band minimum resulting in the S decrease. This result demonstrates that we experimentally clarified the actual strain effect in epitaxial films. These results highlight that in terms of S , $\text{Si}_{1-x}\text{Ge}_x$ samples with smaller x and ϵ values are better due to their larger effective DOS.

Figure 2(e) summarizes the $S^2\sigma$ values of the samples. The Ge samples exhibited the highest $S^2\sigma$ values ($47 \pm 9 \mu\text{W cm}^{-1} \text{ K}^{-2}$) among the $\text{Si}_{1-x}\text{Ge}_x$ samples. The $S^2\sigma$ value of the present Ge epitaxial film is approximately 1.2 times higher than the reported maximum $S^2\sigma$ values of n -type SiGe-alloy-based bulks³⁴ and polycrystalline SiGe films.¹² This higher $S^2\sigma$ value of the Ge samples is due to the higher value of σ arising from the smaller m_c . On the other hand, for $\text{Si}_{1-x}\text{Ge}_x$ samples except for the case of $x = 1$ (i.e., Ge samples), all the samples exhibited almost the same $S^2\sigma$ values, regardless of x and $\epsilon_{||}$ values. These similar values result from mixed contributions of some factors, such as the strain (high σ and low S) and crystal defects caused by strain relaxation (low σ and S). Furthermore, σ , S , and $S^2\sigma$ of the two-step Ge sample with maximum $S^2\sigma$ ($n \sim 2.8 \times 10^{19} \text{ cm}^{-3}$) in Fig. 2(e) were measured as a function of T in the range between 300 and 400 K (see Fig. S3 in the supplementary material). The decrease in σ with the T increase indicates the degenerate semiconductor, and S increases in a typical trend. As a result, the maximum $S^2\sigma$ value was $\sim 57 \pm 11 \mu\text{W cm}^{-1} \text{ K}^{-2}$ at 400 K. This demonstrates the prospect of the Ge thin films for TEG use in this temperature range near room temperature.

The cross-plane κ values were measured using TDTR (see the supplementary material, Sec. IV).⁴⁵ The undoped one-step $\text{Si}_{0.7}\text{Ge}_{0.3}$ sample (100 nm) exhibited a lower κ value of $\sim 1.8 \pm 0.7 \text{ W m}^{-1} \text{ K}^{-1}$ due to the phonon alloy scattering than the undoped two-step Ge sample ($25 \pm 8 \text{ W m}^{-1} \text{ K}^{-1}$). Next, to investigate the doping effect, the κ values of the doped one-step $\text{Si}_{0.7}\text{Ge}_{0.3}$ sample (100 nm) and the doped two-step Ge sample were measured to be $\sim 1.9 \pm 0.8$ and $\sim 6.5 \pm 1.1 \text{ W m}^{-1} \text{ K}^{-1}$, respectively. The lattice thermal conductivities (κ_{lat}) were found to be $\sim 1.6 \text{ W m}^{-1} \text{ K}^{-1}$ in the doped one-step $\text{Si}_{0.7}\text{Ge}_{0.3}$ sample (100 nm) and $\sim 6.1 \text{ W m}^{-1} \text{ K}^{-1}$ in the doped two-step Ge sample by subtracting the electronic thermal conductivity estimated from the Wiedemann–Franz law with the Lorenz number of $2.44 \times 10^{-8} \Omega \text{ W K}^{-2}$. The similarity between κ and κ_{lat} indicates that the main heat carrier is a phonon. In the case of the Ge films, the P doping reduced κ_{lat} more largely ($\sim 6.1 \text{ W m}^{-1} \text{ K}^{-1}$) than the Ga doping ($\sim 15 \text{ W m}^{-1} \text{ K}^{-1}$)³³ even though the dopant concentration is almost the same ($1\text{--}2 \times 10^{20} \text{ cm}^{-3}$). This supposedly originates from the large mass difference between Ge and P compared to that between Ge and Ga. On the other hand, in the case of the $\text{Si}_{0.7}\text{Ge}_{0.3}$ films, almost no reduction of κ_{lat} was observed upon

doping. This is presumably because phonons are already scattered by the atomic mass difference (alloy scattering) thoroughly before introducing dopants as the atomic mass difference for phonon scattering. In addition, we roughly estimated the in-plane κ values to calculate the values of ZT . It is reported that the in-plane and cross-plane κ values were measured to be two times different in the polycrystalline $\text{Si}_{0.7}\text{Ge}_{0.3}$ film, where the composing grains have a lateral size of ~ 270 nm and a vertical thickness of ~ 1.2 μm .¹⁴ Considering the relationship between the domain shape anisotropy and the κ anisotropy (two times different values), the in-plane κ values of the present SiGe and Ge epitaxial films were assumed to be approximately two times larger than the cross-plane κ . Thus, using the estimated in-plane κ and maximum $S^2\sigma$ in Fig. 2(e), the in-plane ZT values of the SiGe and Ge epitaxial films were expected to be ~ 0.15 and ~ 0.11 at room temperature, respectively.

Here, it should be noted that the κ values of the epitaxial $\text{Si}_{1-x}\text{Ge}_x$ films ($\sim 1.8 \pm 0.7$ $\text{W m}^{-1} \text{K}^{-1}$ for undoped films) are much lower than those of bulk $\text{Si}_{0.7}\text{Ge}_{0.3}$ (~ 8 $\text{W m}^{-1} \text{K}^{-1}$)²⁸ and bulk Ge (~ 60 $\text{W m}^{-1} \text{K}^{-1}$)²⁷ and close to the value of amorphous Si (~ 1 – 2 $\text{W m}^{-1} \text{K}^{-1}$)^{46–48} although this sample is simply an epitaxial film without nanostructures. Thus, in terms of the κ value, $\text{Si}_{1-x}\text{Ge}_x$ films are more advantageous than Ge films. Therefore, in the situations where ΔT is variable, such as TFTEG for the internet of human, $\text{Si}_{1-x}\text{Ge}_x$ samples with ultralow κ are better for TFTEG use, while high power factor Ge films can also be advantageous for TFTEG applications by applying the nanostructuring technique.

We fabricated a preliminary TFTEG using a two-step Ge sample and investigated its operation under a constant ΔT situation. As shown in the photograph of the Ge film TEG [Fig. 3(a)], the TFTEG composed of 10 stripe structures was well fabricated. Figure 3(b) shows the output voltage (V_{out}) and output power (P_{out}) as a function of the output current (I_{out}) under ΔT values of 4, 12, and 20 K, indicating that P_{out} is roughly proportional to ΔT^2 . The preliminary TFTEG generated a maximum P_{out} value of ~ 0.10 $\mu\text{W cm}^{-2}$ when applying a ΔT value of 20 K, demonstrating the operation of the Ge film TEG.

In conclusion, we presented the material design of $\text{Si}_{1-x}\text{Ge}_x$ epitaxial films/Si for the TFTEG by investigating their TE properties. We fabricated $\text{Si}_{1-x}\text{Ge}_x$ epitaxial films with various x values and strain using two types of growth methods. Ge films exhibited the highest $S^2\sigma$ of ~ 47 $\mu\text{W cm}^{-1} \text{K}^{-2}$ among $\text{Si}_{1-x}\text{Ge}_x$ epitaxial films, which is higher than the reported maximum $S^2\sigma$ values of n-type SiGe alloys.³⁴ $\text{Si}_{0.7}\text{Ge}_{0.3}$ films exhibited the ultralow κ of ~ 2 $\text{W m}^{-1} \text{K}^{-1}$ even without nanostructures. It was found that $\text{Si}_{1-x}\text{Ge}_x$ epitaxial films with

ultralow κ are suitable for TFTEGs under changeable ΔT situations, while Ge epitaxial films with higher $S^2\sigma$ are also suitable after nanostructuring. We tested the operation of a preliminary TFTEG using a Ge film with a higher $S^2\sigma$ and demonstrated that $\text{Si}_{1-x}\text{Ge}_x$ epitaxial TE films/Si can be promising TE materials suitable for industrial applications.

See the [supplementary material](#) for reciprocal lattice space mapping of $\text{Si}_{1-x}\text{Ge}_x$ films, semi-empirical electrical conductivity and mobility of bulk $\text{Si}_{1-x}\text{Ge}_x$ and Ge, temperature dependence of thermoelectric properties, and TDTR measurements and analysis.

This work was supported by Grant-in-Aid for Scientific Research A (No. 19H00853), Grant-in-Aid for Exploratory Research (No. 19K22110), Grant-in-Aid for Scientific Research B (No. 19H02087), and Grant-in-Aid for JSPS Research fellow (No. 18J20160) from JSPS KAKENHI, Japan. This work was also supported in part by JST CREST Grant No. JPMJCR1524. We thank the members of the Comprehensive Analysis Center, ISIR, Osaka University, for the XRD data.

DATA AVAILABILITY

The data that support the findings of this study are available within the article and its [supplementary material](#).

REFERENCES

- T. Huesgen, P. Woias, and N. Kockmann, *Sens. Actuators, A* **145–146**, 423 (2008).
- P. Fan, Z. Zheng, Z. Cai, T. Chen, P. Liu, X. Cai, D. Zhang, G. Liang, and J. Luo, *Appl. Phys. Lett.* **102**, 033904 (2013).
- K. Takahashi, H. Ikenoue, M. Sakashita, O. Nakatsuka, S. Zaima, and M. Kurosawa, *Appl. Phys. Express* **12**, 051016 (2019).
- M. Takashiri, T. Borca-Tasciuc, A. Jacquot, K. Miyazaki, and G. Chen, *J. Appl. Phys.* **100**, 054315 (2006).
- G. J. Snyder and E. S. Toberer, *Nat. Mater.* **7**, 105 (2008).
- B. Poudel, Q. Hao, Y. Ma, Y. Lan, A. Minnich, B. Yu, X. Yan, D. Wang, A. Muto, D. Vashaee, X. Chen, J. Liu, M. S. Dresselhaus, G. Chen, and Z. Ren, *Science* **320**, 634 (2008).
- A. I. Hochbaum, R. Chen, R. D. Delgado, W. Liang, E. C. Garnet, M. Najarian, A. Majumdar, and P. Yang, *Nature* **451**, 163 (2008).
- G. Joshi, H. Lee, Y. Lan, X. Wang, G. Zhu, D. Wang, R. W. Gould, D. C. Cuff, M. Y. Tang, M. S. Dresselhaus, G. Chen, and Z. Ren, *Nano Lett.* **8**, 4670 (2008).
- M. Zebarjadi, G. Joshi, G. Zhu, B. Yu, A. Minnich, Y. Lan, X. Wang, M. Dresselhaus, Z. Ren, and G. Chen, *Nano Lett.* **11**, 2225 (2011).
- N. Neophytou, X. Zianni, H. Kosina, S. Frabboni, B. Lorenzi, and D. Narducci, *Nanotechnology* **24**, 205402 (2013).
- Y. Nakamura, M. Isogawa, T. Ueda, S. Yamasaka, H. Matsui, J. Kikkawa, S. Ikeuchi, T. Oyake, T. Hori, J. Shiomi, and A. Sakai, *Nano Energy* **12**, 845 (2015).
- A. Nozariasbmarz, A. T. Rad, Z. Zamanipour, J. S. Krasinski, L. Tayebi, and D. Vashaee, *Scr. Mater.* **69**, 549 (2013).
- S. Yamasaka, K. Watanabe, S. Sakane, S. Takeuchi, A. Sakai, K. Sawano, and Y. Nakamura, *Sci. Rep.* **6**, 22838 (2016).
- J. Lu, R. Guo, and B. Huang, *Appl. Phys. Lett.* **108**, 141903 (2016).
- Y. Nakamura, *Sci. Technol. Adv. Mater.* **19**, 31 (2018).
- T. Ishibe, A. Tomeda, K. Watanabe, Y. Kamakura, N. Mori, N. Naruse, Y. Mera, Y. Yamashita, and Y. Nakamura, *ACS Appl. Mater. Interfaces* **10**, 37709 (2018).
- S. Sakane, T. Ishibe, T. Hinakawa, N. Naruse, Y. Mera, Md. M. Alam, K. Sawano, and Y. Nakamura, *Appl. Phys. Lett.* **115**, 182104 (2019).
- T. Taniguchi, T. Ishibe, N. Naruse, Y. Mera, Md. M. Alam, K. Sawano, and Y. Nakamura, *ACS Appl. Mater. Interfaces* **12**, 25428 (2020).

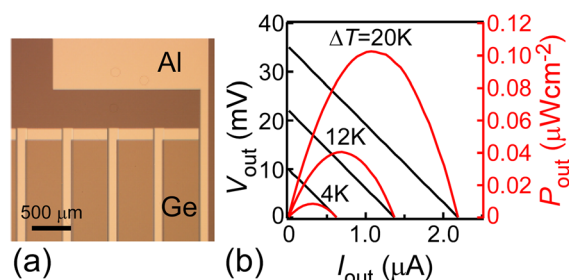


FIG. 3. (a) Photograph of the TFTEG fabricated using a Ge epitaxial film. (b) V_{out} and P_{out} of the TFTEG as a function of I_{out} under $\Delta T = 4, 12$, and 20 K.

- ¹⁹P. Chen, J. J. Zhang, J. P. Feser, F. Pezzoli, O. Moutanabbir, S. Cecchi, G. Isella, T. Gemming, S. Baunack, G. Chen, O. G. Schmidt, and A. Rastelli, *J. Appl. Phys.* **115**, 044312 (2014).
- ²⁰S. Yamasaka, Y. Nakamura, T. Ueda, S. Takeuchi, and A. Sakai, *Sci. Rep.* **5**, 14490 (2015).
- ²¹X. Huang, S. Gluchko, R. Anufriev, S. Volz, and M. Nomura, *ACS Appl. Mater. Interfaces* **11**, 34394 (2019).
- ²²Y. Nakamura, A. Masada, and M. Ichikawa, *Appl. Phys. Lett.* **91**, 013109 (2007).
- ²³Y. Nakamura, A. Murayama, R. Watanabe, T. Iyoda, and M. Ichikawa, *Nanotechnology* **21**, 095305 (2010).
- ²⁴J. Maire, R. Anufriev, R. Yanagisawa, A. Ramiere, S. Volz, and M. Nomura, *Sci. Adv.* **3**, e1700027 (2017).
- ²⁵K. Takahashi, M. Fujikane, Y. Liao, M. Kashiwagi, T. Kawasaki, N. Tambo, S. Ju, Y. Naito, and J. Shiomi, *Nano Energy* **71**, 104581 (2020).
- ²⁶T. Ishibe, Y. Maeda, T. Terada, N. Naruse, Y. Mera, E. Kobayashi, and Y. Nakamura, *Sci. Technol. Adv. Mater.* **21**, 195 (2020).
- ²⁷T. H. Geballe and G. W. Hull, *Phys. Rev.* **94**, 1134 (1954).
- ²⁸J. P. Dismukes, L. Ekstrom, E. F. Steigmeier, I. Kudman, and D. S. Beers, *J. Appl. Phys.* **35**, 2899 (1964).
- ²⁹F. Murphy-Armando, *J. Appl. Phys.* **126**, 215103 (2019).
- ³⁰T. Koga, S. B. Cronin, M. S. Dresselhaus, J. L. Liu, and K. L. Wang, *Appl. Phys. Lett.* **77**, 1490 (2000).
- ³¹Y. Ezzahri, G. Zeng, K. Fukutani, Z. Bian, and A. Shakouri, *Microelectron. J.* **39**, 981 (2008).
- ³²L. F. Llin, A. Samarelli, S. Cecchi, T. Etzelstorfer, E. M. Gubler, D. Chrastina, G. Isella, J. Stangl, J. M. R. Weaver, P. S. Dobson, and D. J. Paul, *Appl. Phys. Lett.* **103**, 143507 (2013).
- ³³T. Taniguchi, T. Ishibe, H. Miyamoto, Y. Yamashita, and Y. Nakamura, *Appl. Phys. Express* **11**, 111301 (2018).
- ³⁴O. Yamashita and N. Sadatomi, *J. Appl. Phys.* **88**, 245 (2000).
- ³⁵K. Lyutovich, J. Werner, M. Oehme, E. Kasper, and T. Perova, *Mater. Sci. Semicond. Process.* **8**, 149 (2005).
- ³⁶J. M. Hartmann, A. Abbadie, and S. Favier, *J. Appl. Phys.* **110**, 083529 (2011).
- ³⁷M. Uenuma, Y. Ishikawa, and Y. Uraoka, *Appl. Phys. Lett.* **107**, 073503 (2015).
- ³⁸D. B. Cuttriss, *Bell Syst. Tech. J.* **40**, 509 (1961).
- ³⁹G. A. Slack and M. A. Hussain, *J. Appl. Phys.* **70**, 2694 (1991).
- ⁴⁰M. V. Fischetti and S. E. Laux, *J. Appl. Phys.* **80**, 2234 (1996).
- ⁴¹L. Yang, J. R. Watling, R. C. W. Wilkins, M. Boriçi, J. R. Barker, A. Asenov, and S. Roy, *Semicond. Sci. Technol.* **19**, 1174 (2004).
- ⁴²T. J. Scheidmantel, C. Ambrosch-Draxl, T. Thonhauser, J. V. Badding, and J. O. Sofo, *Phys. Rev. B* **68**, 125210 (2003).
- ⁴³D. Chattopadhyay and H. J. Queisser, *Rev. Mod. Phys.* **53**, 745 (1981).
- ⁴⁴M. Ershov and V. Ryzhii, *Jpn. J. Appl. Phys., Part 1* **33**, 1365 (1994).
- ⁴⁵Y. Yamashita, K. Honda, T. Yagi, J. Jia, N. Taketoshi, and Y. Shigesato, *J. Appl. Phys.* **125**, 035101 (2019).
- ⁴⁶D. G. Chahill, S. K. Watson, and R. O. Pohl, *Phys. Rev. B* **46**, 6131 (1992).
- ⁴⁷D. G. Chahill, M. Katiyar, and J. R. Abelson, *Phys. Rev. B* **50**, 6077 (1994).
- ⁴⁸Y. He, D. Donadio, and G. Galli, *Appl. Phys. Lett.* **98**, 144101 (2011).